

Signatures of coupling between spin waves and Dirac fermions in YbMnBi₂

A. Sapkota,¹ L. Classen,^{1,2} M. B. Stone,³ A. T. Savici,³ V. O. Garlea,³
Aifeng Wang,^{1,*} J. M. Tranquada,¹ C. Petrovic,¹ and I. A. Zaliznyak^{1,†}

¹*Condensed Matter Physics and Materials Science Division,
Brookhaven National Laboratory, Upton, NY 11973, USA*

²*School of Physics and Astronomy, University of Minnesota, Minneapolis, MN 55415, USA*

³*Neutron Scattering Division, Oak Ridge National Laboratory, Oak Ridge, TN 37831, USA*

(Dated: May 2, 2022)

We present inelastic neutron scattering (INS) measurements of magnetic excitations in YbMnBi₂, which reveal features consistent with a direct coupling of magnetic excitations to Dirac fermions. In contrast with the large broadening of magnetic spectra observed in antiferromagnetic metals such as the iron pnictides, here the spin waves exhibit a small but resolvable intrinsic width, consistent with our theoretical analysis. The subtle manifestation of spin-fermion coupling is a consequence of the Dirac nature of the conduction electrons, including the vanishing density of states near the Dirac points. Accounting for the Dirac fermion dispersion specific to YbMnBi₂ leads to particular signatures, such as the nearly wave-vector independent damping observed in the experiment.

Dirac and Weyl materials exhibit many exotic and novel quantum phenomena that are both of fundamental and potential technological interest [1–4]. This class of materials encompasses a wide range of condensed matter systems including graphene, *d*-wave superconductors, and topological insulators and semimetals [1]. The name is derived from their low-energy electronic dispersions that can be described by a relativistic Dirac or Weyl Hamiltonian. The linear variation of energy as a function of wave vector about a Dirac node is a universal feature that leads to novel behaviors such as suppression of backscattering, high carrier mobility, impurity-induced resonant states, spin-polarized transport, and the unusual quantum Hall effect [1–6]. Furthermore, interaction of these low-energy Dirac/Weyl fermions with other degrees of freedom leads to novel physics with technological potential [2, 7, 8]. Hence, understanding coupling of Dirac fermions with other quantum excitations, such as spin waves, is a topic of great current interest.

From this perspective, 112 ternary bismuthides (*R, A*)MnBi₂ (*R* = Rare-earth, *A* = Alkaline-earth: Ca, Sr) represent a particularly interesting family where both magnetism and Dirac fermions coexist, providing a platform to study their interplay [3, 4, 9–11]. In these materials, the Dirac bands and the magnetic order are associated with distinct square-net layers: conducting Bi layers and magnetic MnBi layers separated by layers of *R, A*, as shown in Fig. 1(a) of Ref. 12. While indirect experimental evidence of a coupling between conduction electrons and magnetic Mn ions is provided by the impact of the magnetic order on electrical transport in CaMnBi₂ [11], inelastic neutron scattering measurements on Sr/CaMnBi₂ detect no decay of spin waves into particle-hole excitations that would substantiate the coupling [13]. The spin waves appear undamped, no different from the case of an insulator, CaMn₂Sb₂ [14].

RMnBi₂ systems were suggested as possible candidates where coupling of Dirac fermions with spins could be

significant. EuMnBi₂ and YbMnBi₂ are two such recently discovered materials [12]. YbMnBi₂ is particularly interesting because of its possible link with type-II Weyl physics with broken time-reversal symmetry [15–17]. In addition, it holds promise because the ferromagnetic stacking of Mn moments along the *c*-axis, similar to CaMnBi₂, suggests that an interlayer exchange interaction can be mediated by Dirac bands [11, 13]. However, the question remains, is there any signature of coupling/entanglement with Dirac fermions in the magnetic excitation spectrum of YbMnBi₂? If the coupling does exist, what is the magnitude of this coupling and will magnetic excitations exhibit anomalous broadening, as found in other metallic magnets [13, 18]?

Here, we present the results of INS measurements performed on YbMnBi₂ at 4 different temperatures, spanning the Néel temperature, T_N . We show that the magnetic excitations are well-defined spin waves below T_N , becoming dispersive paramagnons (similar to spin waves) just above T_N , and both can be described with a local-moment Heisenberg model. From our analysis, we extract a damping parameter associated with the observed broadening of the magnetic excitations and compare it to that of both metallic and insulating antiferromagnets. We find that the damping is consistent with the decay of magnetic excitations into Dirac particle-hole pairs and is very different from that usually found in metallic antiferromagnets, such as iron pnictides [18–23]. Unlike electrons in conventional itinerant magnets, the Dirac fermions are stable against antiferromagnetic fluctuations due to their vanishing density of states near the Dirac points, which suppresses the effects of spin-fermion interactions. In addition, Dirac fermions and spin waves in YbMnBi₂ are spatially separated degrees of freedom that primarily propagate in different layers, which further inhibits the coupling. Nevertheless, we show that the damping measured in our INS experiment is consistent with a simple spin-fermion coupling model, which

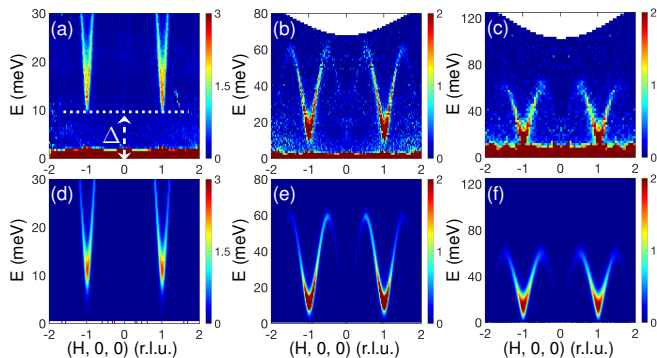


FIG. 1. Spin waves in YbMnBi₂ in the antiferromagnetic state. (a)–(c) INS spectra showing dispersion along $(H, 0, 0)$ direction measured at $T = 4$ K with incident energies $E_i = 35, 100$ and 200 meV, respectively. Dashed line in (a) indicates the spin gap, Δ (cf Table I and Fig. S6). (d)–(f) INS spectra calculated using spin wave dispersion and Eq. (1), with the best fit parameters listed in Table I. For fitting, only the data measured with $E_i = 100$ meV shown in Fig. 2 were used [24]. Intensity scales shown in the colorbars are in arbitrary units and absolute magnitude differs among different E_i .

accounts for the specifics of Dirac dispersion in YbMnBi₂ [16], in the framework of the random phase approximation (RPA). From our experimental results, we determine the coupling constant in this model, which is directly proportional to the experimental damping parameter.

Single crystals of YbMnBi₂ were grown from Bi flux as described in Ref. 12. YbMnBi₂ orders antiferromagnetically below $T_N \approx 290$ K, with an ordered moment of $4.3\mu_B$ at 4 K [12, 25, 26]. INS measurements were performed at SEQUOIA (Figs. 1–3) and HYSPEC [24] spectrometers at the Spallation Neutron Source, Oak Ridge National Laboratory. Four single crystals with the total mass of ≈ 1.8 g were co-aligned in the $(H, 0, L)$ horizontal scattering plane, with the effective mosaic spread of $\lesssim 0.8^\circ$ full-width at half-maximum (FWHM). The measurements were carried out with incident energies $E_i = 35, 100$ and 200 meV at $T = 4, 150, 270$ and 320 K by rotating the sample about its vertical axis in 1° steps over a 270° range (70° for 150 K). Throughout the paper, we index momentum transfer, $\mathbf{Q} = (H, K, L)$ in reciprocal lattice units (rlu) of the $P4/nmm$ lattice, $a = b = 4.48$ Å, $c = 10.8$ Å [12].

Figure 1 (a)–(c) present inelastic neutron scattering spectra for YbMnBi₂ in the antiferromagnetic (AFM) phase at $T = 4$ K, which probe the spin wave dispersion along $(H, 0, 0)$ symmetry direction. Magnetic excitations are well-defined and sharp in both \mathbf{Q} and E , indicating the presence of conventional spin-waves consistent with the local-moment description. The spin waves originate from $\mathbf{Q}_{\text{AFM}} = (\pm 1, 0, 0)$, as expected for a Néel-type magnetic order in YbMnBi₂ [12]. Figure 1(a) demonstrates the presence of a spin-gap, $\Delta \gtrsim 10$ meV. The spin-wave dispersion bandwidth along $(H, 0, 0)$ is ≈ 50 meV,

which is similar to the values measured in CaMnBi₂ and SrMnBi₂ [13].

To uncover the coupling, we perform a quantitative analysis of the measured spectral function in the framework of a $J_1 - J_2 - J_c$ Heisenberg model (J_1, J_2 and J_c are the nearest and next-nearest neighbor in-plane and the inter-plane exchange interaction, respectively). In order to account for potential spin-wave damping, we use a damped-harmonic-oscillator (DHO) representation of the dynamical spin correlation function, $S(\mathbf{Q}, E)$,

$$S(\mathbf{q} + \mathbf{Q}_{\text{AFM}}, E) = S_{\text{eff}} \frac{1}{\pi} \frac{2(A_{\mathbf{q}} - B_{\mathbf{q}})}{1 - e^{-E/k_B T}} \times A \frac{\gamma E}{[E^2 - E_{\mathbf{q}}^2]^2 + (\gamma E)^2}. \quad (1)$$

Here, γ is the damping parameter (FWHM), k_B is the Boltzmann constant, S_{eff} is the effective fluctuating spin, and prefactor A ensures that the DHO spectral function is normalized to 1 (for $T, \gamma \rightarrow 0, A \rightarrow 1$) [24]. At $T \ll T_N$, spin wave theory gives $A_{\mathbf{q}} = 2S[2J_1 - 2J_2[\sin^2(\pi H) + \sin^2(\pi K)] - 2J_c \sin^2(\pi L) - D]$, $B_{\mathbf{q}} = 4S J_1 \cos(\pi H) \cos(\pi K)$, and $E_{\mathbf{q}}^2 = A_{\mathbf{q}}^2 - B_{\mathbf{q}}^2$.

We fit the data at each temperature using the cross-section given by Eq. (1) convolved with the instrumental resolution. The resulting fits are shown side-by-side with the data in Figures 1 and 2 (additional details provided in [24]). The best fit values thus obtained are shown in Table I. We find that the in-plane exchange parameters are nearly temperature-independent. The spin gap, Δ , which is determined by the effective uniaxial-anisotropy parameter, SD , decreases with increasing temperature and approaches zero above T_N .

Our crucial finding is a small and approximately \mathbf{Q} -independent damping parameter, γ , which is present at all temperatures. It increases by roughly a factor of 5 in the paramagnetic state, just above T_N , still remaining nearly \mathbf{Q} -independent. The \mathbf{Q} independence of γ is also supported by a supplementary analysis where energy (constant- \mathbf{Q}) cuts were fit with a DHO (Eq. (1), Eq. (S5) [24]) as illustrated in Fig. 3 (a)–(d). The static structure factor, $S(\mathbf{Q})$, and the correlation length, ξ , were also obtained in this procedure [24].

A comparison of γ to both the metallic/itinerant and local-moment magnetism scenarios unfolds the nature of spin-fermion interaction in YbMnBi₂. In itinerant antiferromagnets, such as iron and cobalt pnictide compounds, the signature of spin-fermion coupling in the magnetic excitation spectra is found in the form of anomalous broadening of spin waves due to their decay into particle-hole pairs. As a result, a large and anisotropic γ , increasing towards the zone boundary, is observed in the magnetically ordered state [21] and broad, diffusive-type spin fluctuations in the paramagnetic (PM) state [22, 23, 27, 28]. No such strong broadening in the antiferromagnetic state is seen in our

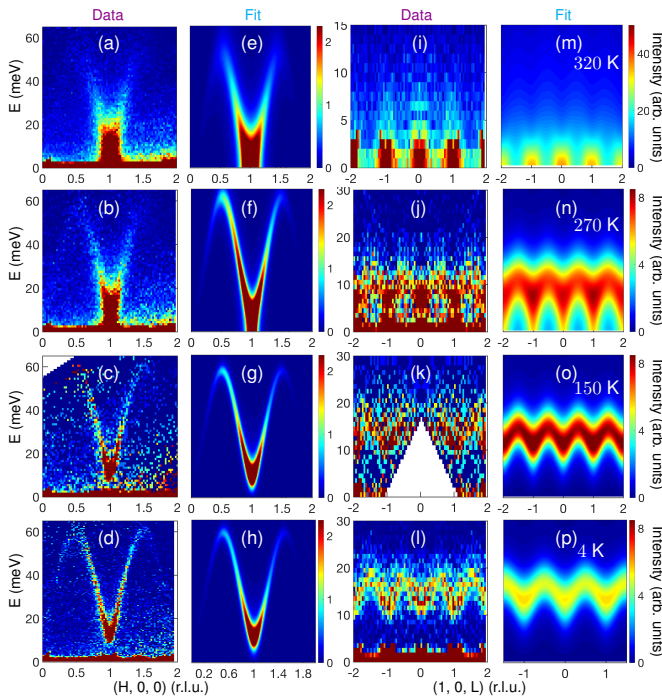


FIG. 2. INS spectra measured on YbMnBi₂ with $E_i = 100$ meV at $T = 320$ K, 270 K, 150 K and 4 K, illustrating the spin-wave dispersions along two symmetry directions, $(H, 0, 0)$ (a–d) and $(0, 0, L)$ (i–l). (e–h) and (m–p), INS spectra calculated using DHO, Eq. (1), for the same wave vectors as the data, using the results of fits given in Table I, and corrected for the instrument resolution (see [24] for details).

data, where γ is small and approximately \mathbf{Q} -independent [Table I, Fig. 3 (a)–(d)]. At the other extreme, there are no electronic excitations with which spin waves can interact in antiferromagnetic insulators. A comparison with relevant Mn-based compounds [14, 29] shows that the damping in these insulators is at least an order of magnitude smaller than what we find in YbMnBi₂.

We now calculate the correction to the spin susceptibility through coupling to the Dirac fermions within RPA and show that the observed damping is consistent with theoretical expectations for YbMnBi₂. The linear electronic dispersion in YbMnBi₂ predominantly arises from two-dimensional bands of Bi $6p$ states, which cross near the Fermi level [16]. If spin-orbit coupling and antiferromagnetism of YbMnBi₂ are neglected, the crossing is along an extended nodal line which originates in the staggered geometry of Yb with respect to the Bi square net [16, 30]. Although this nodal line reduces to a point upon inclusion of spin-orbit coupling and perfect antiferromagnetism of Mn atoms, four linear crossings (above the Fermi energy) are preserved in the Brillouin zone of YbMnBi₂ [16]. Importantly, as a “memory” of the nodal line, the resulting Fermi velocities are very anisotropic, with $v_{F\perp} \approx 9$ eVÅ perpendicular to the nodal line direction and $v_{F\parallel} \approx 0.043$ eVÅ along it [16, 17]. This extreme difference in the velocities will turn out to en-

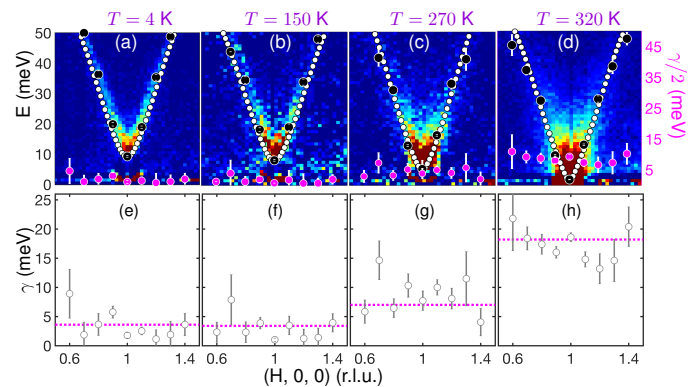


FIG. 3. \mathbf{Q} and temperature dependence of damping parameter, γ , and low-energy part of spin wave dispersion, $E_{\mathbf{q}}$. The under-damped spin wave exists where $E_{\mathbf{q}} > \gamma/2$. (a)–(d) \mathbf{Q} -independent damping parameter (magenta solid circles with white error bars showing one standard deviation) obtained from fitting 1D energy cuts using DHO response at $T = 4$ K, 150 K, 270 K and 320 K, respectively. Black circles show the corresponding spin wave energy, $E_{\mathbf{q}}$, which was fitted for all temperatures. White circles illustrate the dispersion obtained using the parameters in Table I for the corresponding temperature. (e)–(h) Open circles are fitted values from 1D data and magenta dashed lines are for 2D data given in Table I.

able low-energy scattering processes between spins and Dirac fermions that explain the observed damping.

We model the described system of spins and conduction electrons in YbMnBi₂ via the action,

$$\begin{aligned}
 S = & \int \frac{d^d p}{(2\pi)^d} \sum_{\eta=\pm} [\psi_{\eta}^{\dagger}(p) (ip_0 + \eta v_{1,\eta} \tau_x p_1 + v_{2,\eta} \tau_y p_2) \psi_{\eta}(p)] \\
 & + \frac{g}{2} \int \frac{d^d p}{(2\pi)^d} \int \frac{d^d q}{(2\pi)^d} [\mathbf{S}_{\mathbf{q}} \psi_{+}^{\dagger}(p) \boldsymbol{\sigma} \otimes \tau_x \psi_{-}(p-q) + \text{h.c.}] \\
 & + \int \frac{d^d q}{(2\pi)^d} \mathbf{S}_{\mathbf{q}} \chi_0^{-1} \mathbf{S}_{-\mathbf{q}}, \quad (2)
 \end{aligned}$$

which describes two Dirac cones at \mathbf{p}_{η} [$\eta = \pm$, see Fig. 4(a)] with anisotropic velocities, $v_{1,+} = v_{2,-} = v_{\perp}$ and $v_{1,-} = v_{2,+} = v_{\parallel}$, rotated with respect to each other ($v_{\parallel}/v_{\perp} \approx 0.005$ in YbMnBi₂). We use rotated coordinates, $p_{1,2} = (p_x \pm p_y)/\sqrt{2}$. Pauli matrices (τ) σ act on (pseudo-)spin, respectively. The Mn spin waves are represented by the three-component boson field, \mathbf{S} . Their dynamical susceptibility is given by the bare expression, without damping, $\chi_0^{-1}(E) = E^2 - E_{\mathbf{q}}^2$ [cf. Eq. (1)].

For simplicity, we perform calculations at $T = 0$ and in $d = 2 + 1$ dimensions. We assume that the Dirac points have opposite chirality, as was found in the related compound, SrMnBi₂ [30], and we consider a coupling, $\propto g$, which does not break chiral symmetry. In the coupling term in Eq. (2), we measure the wave vector transfer relative to the antiferromagnetic wave vector, $\mathbf{Q}_{\text{AFM}} = \mathbf{p}_{+} - \mathbf{p}_{-}$, which happens to connect the centers of the Dirac cones [see Fig. 4(a)]. Because of the

TABLE I. Exchange coupling, uniaxial anisotropy, and damping parameters for YbMnBi₂ obtained from fitting two-dimensional data shown in Fig. 2.

	$T = 4$ K	$T = 150$ K	$T = 270$ K	$T = 320$ K
SJ_1 (meV)	25.2 ± 0.2	24.3 ± 0.3	27.1 ± 0.5	25.0 ± 0.4
SJ_2/SJ_1	0.40 ± 0.01	0.40 ± 0.01	0.42 ± 0.01	0.44 ± 0.01
$ SJ_c /SJ_1$	0.0052 ± 0.0001	0.0041 ± 0.0001	0.0019 ± 0.0001	0.0016 ± 0.0001
SD (meV)	-0.20 ± 0.01	-0.16 ± 0.01	-0.06 ± 0.02	-0.003 ± 0.001
Δ (meV)	9.0 ± 0.2	7.9 ± 0.2	5.3 ± 0.8	1 ± 1
γ (meV)	3.6 ± 0.2	3.4 ± 0.2	7.2 ± 1.0	18.2 ± 0.6

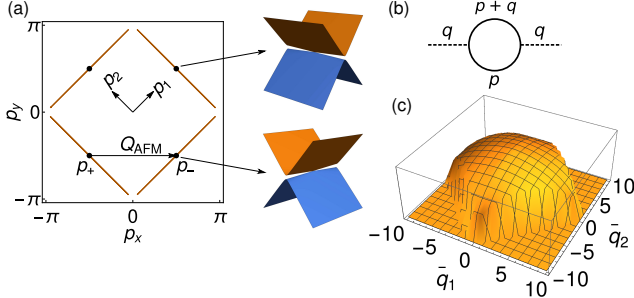


FIG. 4. (a) The Fermi surface resulting from the anisotropic Dirac cones and a shift of the crossing away from the Fermi surface. The Dirac cones are rotated with respect to each other as sketched to the right. The centers of the \mathbf{p}_+ and \mathbf{p}_- cones are connected by the antiferromagnetic wave vector $\mathbf{Q}_{AFM} = (\pi, 0)$. (b) Diagrammatic representation of the leading correction to the spin susceptibility through coupling to the Dirac electrons. Solid lines are Dirac propagators, dashed lines are spin waves. (c) The polarization $\text{Im}\Pi(E, \bar{q}_1, \bar{q}_2)$ obtained by numerical integration for an energy $E > \sqrt{2}v_{\parallel}q$ and $v_{\parallel}/v_{\perp} = 0.005$ as function of $\bar{q}_i = v_{\perp}q_i$.

large anisotropy, the elliptical Fermi surface is extremely elongated and appears very similar to a true nodal line.

The leading correction to the bare susceptibility due to coupling to the Dirac electrons renormalizes the spin susceptibility via the polarization, $\chi^{-1} = \chi_0^{-1} - \Pi$, Fig. 4(b). As the coupling is small and the semimetallic state in 2D Dirac materials is known to be stable due to a vanishing density of states at the Dirac points, we expect the second-order approximation for Π to adequately capture the damping effects,

$$\Pi(E, \mathbf{q}) = -\frac{g^2}{2} \int \frac{d^d p}{(2\pi)^d} \text{Tr}[G_+(p_0, \mathbf{p})\tau_x G_-(p_0 + E, \mathbf{p} + \mathbf{q})\tau_x], \quad (3)$$

with Dirac propagators, $G_{\eta}(p_0, \mathbf{p}) = (-ip_0 + \eta v_{1,\eta}\tau_x p_1 + v_{2,\eta}\tau_y p_2)/(p_0^2 + v_{1,\eta}^2 p_1^2 + v_{2,\eta}^2 p_2^2)$. The damping can be determined by the imaginary part of the retarded polarization after analytical continuation $ip_0 \rightarrow E + i0^+$. For general v_{\perp}, v_{\parallel} , we obtain a lengthy expression, which can be found in [24].

It is instructive to consider two limits. For isotropic

Dirac cones, $v_{\perp} = v_{\parallel} = v_F$, we find,

$$\text{Im}\Pi^R(E, \mathbf{q}) = \frac{N_f}{8v_F^2} g^2 \text{sign}(E) \sqrt{E^2 - v_F^2 \mathbf{q}^2} \Theta(E^2 - v_F^2 \mathbf{q}^2), \quad (4)$$

where N_f is the number of Dirac cone pairs and Θ is the step function. There are four Dirac points in each Brillouin zone of YbMnBi₂ [16, 17], so $N_f = 2$. Although Eq. (4) has approximately the correct functional form for the DHO ($\text{Im}\Pi^R \approx cE$), the kinematic constraint, $E > v_F|\mathbf{q}|$, usually cannot be satisfied because for most wave vectors electronic energies are much larger than the spin-wave energy. For $E^2 < v_F^2 \mathbf{q}^2$, the polarization function is purely real [31].

The extreme anisotropy of the electronic dispersion in YbMnBi₂ relaxes the kinematic constraint. For momentum transfers along \mathbf{Q}_{AFM} , corresponding to the data shown in Figs. 1–3, the leading order in small $(v_{\parallel}/v_{\perp})$ reads,

$$\text{Im}\Pi^R(E, q) \approx \frac{N_f}{2\pi v_{\perp}^2} g^2 E \Theta(E^2 - 2v_{\parallel}^2 q^2). \quad (5)$$

Accounting for further corrections leads to a weak momentum dependence [24]. The full numerical result for $\text{Im}\Pi^R$ is presented in Fig. 4. The main processes responsible for the enabled damping connect points along the elongated Fermi surfaces so that their energy cost is determined by v_{\parallel} . Due to its remarkable smallness, spin waves are able to excite such particle-hole pairs.

We conclude that the spin wave damping factor in Eq. (1) is given by $\gamma \approx N_f g^2 / (2\pi v_{\perp}^2)$. Thus, using $\gamma \approx 3.6$ meV (Table I), $N_f = 2$, $v_F = 9$ eV \AA , we can estimate the coupling constant, $g \approx 1.0$ eV $^{3/2}$ \AA . The obtained finite value of g quantifies the spin-fermion interaction in YbMnBi₂ and can be used, in future work, to analyze the effect of magnetism on the transport of Dirac electrons in the framework of Eq. (2).

In summary, we measured magnetic excitations in the Dirac material, YbMnBi₂, for temperatures in the range of $0.02 \leq T/T_N \leq 1.10$. The results show dispersing spin waves for all temperatures and their detailed analysis unfolds the nature of spin-fermion coupling between the

magnetic Mn layer and Dirac fermions of the Bi layer. We find a small, but distinct damping of spin waves, which for $T < T_N$ is weakly dependent on temperature and is nearly independent of wave vector. Despite its small magnitude, the observed damping indicates substantial spin-fermion coupling parameter, $g \approx 1.0 \text{ eV}^{3/2}\text{\AA}$, which we quantify by comparing the experiment with the theoretical analysis of model action for Dirac fermions coupled to spin waves, Eq. (2). Therefore, by combining the experimental measurements and theory, we establish the existence of long sought significant spin-fermion coupling in 112 family of Dirac materials.

We thank Alexei Tsvetlik and Michael Scherer for helpful comments and discussions. The work at Brookhaven was supported by the Office of Basic Energy Sciences, U.S. Department of Energy (DOE) under Contract No. DE-SC0012704. This research used resources at the Spallation Neutron Source, a DOE Office of Science User Facility operated by the Oak Ridge National Laboratory. LC acknowledges funding from a Feodor-Lynen research fellowship of the Humboldt foundation.

* Present address: School of Physics, Chongqing University, Chongqing 400044, China

† zaliznyak@bnl.gov

- [1] T. Wehling, A. Black-Schaffer, and A. Balatsky, *Advances in Physics* **63**, 1 (2014).
- [2] M. Khodas, I. A. Zaliznyak, and D. E. Kharzeev, *Phys. Rev. B* **80**, 125428 (2009).
- [3] K. Wang, D. Graf, H. Lei, S. W. Tozer, and C. Petrovic, *Phys. Rev. B* **84**, 220401 (2011).
- [4] A. Wang, D. Graf, L. Wu, K. Wang, E. Bozin, Y. Zhu, and C. Petrovic, *Phys. Rev. B* **94**, 125118 (2016).
- [5] Y. Zhang, Y.-W. Tan, H.-L. Stormer, and P. Kim, *Nat.* **438**, 201 (2005).
- [6] M. Z. Hasan and C. L. Kane, *Rev. Mod. Phys.* **82**, 3045 (2010).
- [7] F. Katmis, V. Lauter, F. S. Nogueira, B. A. Assaf, M. E. Jamer, P. Wei, B. Satpati, J. W. Freeland, I. Eremin, D. Heiman, P. Jarillo-Herrero, and J. S. Moodera, *Nature* **533**, 513 (2016).
- [8] H. Masuda, H. Sakai, M. Tokunaga, Y. Yamasaki, A. Miyake, J. Shiogai, S. Nakamura, S. Awaji, A. Tsukazaki, H. Nakao, Y. Murakami, T.-h. Arima, Y. Tokura, and S. Ishiwata, *Sci. Adv.* **2** (2016), 10.1126/sciadv.1501117.
- [9] J. Park, G. Lee, F. Wolff-Fabris, Y. Y. Koh, M. J. Eom, Y. K. Kim, M. A. Farhan, Y. J. Jo, C. Kim, J. H. Shim, and J. S. Kim, *Phys. Rev. Lett.* **107**, 126402 (2011).
- [10] A. Zhang, C. Liu, C. Yi, G. Zhao, T.-l. Xia, J. Ji, Y. Shi, R. Yu, X. Wang, C. Chen, and Q. Zhang, *Nat. Commun.* **7**, 13833 (2016).
- [11] Y. F. Guo, A. J. Princep, X. Zhang, P. Manuel, D. Khalyavin, I. I. Mazin, Y. G. Shi, and A. T. Boothroyd, *Phys. Rev. B* **90**, 075120 (2014).
- [12] A. Wang, I. Zaliznyak, W. Ren, L. Wu, D. Graf, V. O. Garlea, J. B. Warren, E. Bozin, Y. Zhu, and C. Petrovic, *Phys. Rev. B* **94**, 165161 (2016).
- [13] M. C. Rahn, A. J. Princep, A. Piovano, J. Kulda, Y. F. Guo, Y. G. Shi, and A. T. Boothroyd, *Phys. Rev. B* **95**, 134405 (2017).
- [14] D. E. McNally, J. W. Simonson, J. J. Kistner-Morris, G. J. Smith, J. E. Hassinger, L. DeBeer-Schmitt, A. I. Kolesnikov, I. A. Zaliznyak, and M. C. Aronson, *Phys. Rev. B* **91**, 180407 (2015).
- [15] M. Chinotti, A. Pal, W. J. Ren, C. Petrovic, and L. Degiorgi, *Phys. Rev. B* **94**, 245101 (2016).
- [16] S. Borisenko, D. Evtushinsky, Q. Gibson, A. Yaresko, T. Kim, M. N. Ali, B. Buechner, M. Hoesch, and R. J. Cava, [arXiv:1507.04847](https://arxiv.org/abs/1507.04847) (2015).
- [17] D. Chaudhuri, B. Cheng, A. Yaresko, Q. D. Gibson, R. J. Cava, and N. P. Armitage, *Phys. Rev. B* **96**, 075151 (2017).
- [18] S. O. Diallo, V. P. Antropov, T. G. Perring, C. Broholm, J. J. Pulikkotil, N. Ni, S. L. Bud'ko, P. C. Canfield, A. Kreyssig, A. I. Goldman, and R. J. McQueeney, *Phys. Rev. Lett.* **102**, 187206 (2009).
- [19] R. J. McQueeney, S. O. Diallo, V. P. Antropov, G. D. Samolyuk, C. Broholm, N. Ni, S. Nandi, M. Yethiraj, J. L. Zarestky, J. J. Pulikkotil, A. Kreyssig, M. D. Lumsden, B. N. Harmon, P. C. Canfield, and A. I. Goldman, *Phys. Rev. Lett.* **101**, 227205 (2008).
- [20] D. C. Johnston, *Adv. Phys.* **59**, 803 (2010).
- [21] L. W. Harriger, H. Q. Luo, M. S. Liu, C. Frost, J. P. Hu, M. R. Norman, and P. Dai, *Phys. Rev. B* **84**, 054544 (2011).
- [22] A. Sapkota, B. G. Ueland, V. K. Anand, N. S. Sangeetha, D. L. Abernathy, M. B. Stone, J. L. Niedziela, D. C. Johnston, A. Kreyssig, A. I. Goldman, and R. J. McQueeney, *Phys. Rev. Lett.* **119**, 147201 (2017).
- [23] A. Sapkota, P. Das, A. E. Böhmer, B. G. Ueland, D. L. Abernathy, S. L. Bud'ko, P. C. Canfield, A. Kreyssig, A. I. Goldman, and R. J. McQueeney, *Phys. Rev. B* **97**, 174519 (2018).
- [24] See supplementary materials for additional details.
- [25] K. Wang, D. Graf, L. Wang, H. Lei, S. W. Tozer, and C. Petrovic, *Phys. Rev. B* **85**, 041101 (2012).
- [26] I. A. Zaliznyak, A. T. Savici, V. O. Garlea, B. Winn, U. Filges, J. Schneeloch, J. M. Tranquada, G. Gu, A. Wang, and C. Petrovic, *Journal of Physics: Conference Series* **862**, 012030 (2017).
- [27] S. O. Diallo, D. K. Pratt, R. M. Fernandes, W. Tian, J. L. Zarestky, M. Lumsden, T. G. Perring, C. L. Broholm, N. Ni, S. L. Bud'ko, P. C. Canfield, H.-F. Li, D. Vaknin, A. Kreyssig, A. I. Goldman, and R. J. McQueeney, *Phys. Rev. B* **81**, 214407 (2010).
- [28] W. Jayasekara, Y. Lee, A. Pandey, G. S. Tucker, A. Sapkota, J. Lamsal, S. Calder, D. L. Abernathy, J. L. Niedziela, B. N. Harmon, A. Kreyssig, D. Vaknin, D. C. Johnston, A. I. Goldman, and R. J. McQueeney, *Phys. Rev. Lett.* **111**, 157001 (2013).
- [29] S. P. Bayrakci, D. A. Tennant, P. Leininger, T. Keller, M. C. R. Gibson, S. D. Wilson, R. J. Birgeneau, and B. Keimer, *Phys. Rev. Lett.* **111**, 017204 (2013).
- [30] G. Lee, M. A. Farhan, J. S. Kim, and J. H. Shim, *Phys. Rev. B* **87**, 245104 (2013).
- [31] J. González, F. Guinea, and M. A. H. Vozmediano, *Phys. Rev. Lett.* **77**, 3589 (1996).